Dalton Transactions

ROYAL SOCIETY OF CHEMISTRY

PAPER

View Article Online
View Journal | View Issue

Cite this: *Dalton Trans.*, 2025, **54**, 14070

Leveraging anion selection to modulate crystallographic symmetry in Yb(III) single-molecule magnets

Ethan Lowe, [a] Hamish Hourston, [a] Tanu Sharma,[b] Sarah K. Dugmore, [a] Claire Wilson, [a] Gopalan Rajaraman*[b] and Mark Murrie *[a]

Distortions in the local symmetry around Ln(III) ions in SMMs significantly impacts slow magnetic relaxation by introducing transverse crystal field parameters that enhance quantum tunnelling of the magnetisation (QTM). Minimising these distortions, often using macrocyclic or sterically hindered ligands, or by tuning intermolecular interactions, is essential for suppressing QTM. A less-explored strategy involves aligning the molecular symmetry elements within the crystal lattice to generate a high-symmetry crystal lattice with symmetry enforced bond angles and lengths. Here, we demonstrate that aligning the S_4 axes of $[YbCl_2(Ph_3AsO)_4]^+$ and $[BPh_4]^-$ in $[YbCl_2(Ph_3AsO)_4]BPh_4$ (**1**) enforces tetragonal symmetry and a strict 180° Cl–Yb–Cl angle. In contrast, $[YbCl_2(Ph_3AsO)_4]PF_6$ (**2**) does not possess aligned molecular rotational axes and therefore lacks the crystallographically enforced symmetry leading to a smaller Cl–Yb–Cl angle. While both compounds exhibit similar slow relaxation of the magnetisation, due to efficient Raman relaxation processes, **2** shows a significant decrease in the *ab initio* calculated collinearity of the anisotropy axes of the excited Kramers doublets, alongside a change in the ground $m_J = \pm 7/2$ state composition, with an increased admixture of the $m_J = \pm 1/2$ states. These findings highlight the potential of crystallographically enforced symmetry in designing high-performance Yb(III)-based SMMs.

Received 3rd July 2025,
Accepted 20th August 2025

DOI: 10.1039/d5dt01565k

rsc.li/dalton

Introduction

Lanthanide ions have come to dominate the field of single-molecule magnets (SMMs) producing large magnetisation reversal (U_{eff}) barriers, extremely slow magnetic relaxation times and large coercive fields.[1–3] However, within the large family of Ln(III) metal ions, the field is saturated with Dy(III),[4–6] Tb(III)[7,8] and Er(III)[9,10] SMMs,[11] accompanied by a small number of complexes containing other Ln(III) ions.[12,13] Tuning the ligand field of these other Ln(III) ions, to enhance slow magnetic relaxation, has become a key area of interest for obtaining new multifunctional SMMs.[14–16]

The time reversal symmetry imposed in Kramers ions results in the generation of a bistable ground state, irrespective of the ligand field.[17] As such, this property gives rise to a much greater number of SMMs based on Kramers ions, due to the flexibility of available ligand fields and geometries.[11] However, the Kramers ion Yb(III) presents an interesting case. Despite its Kramers nature there is only one known example of a Yb(III) SMM displaying slow magnetic relaxation without the presence of an applied dc field.[18] Furthermore, this example was only achieved through isotopic enrichment using ^{174}Yb(III), which possesses a nuclear spin $I = 0$. This suggests that Yb(III) is an unusual case among Ln(III) ions and may be highly susceptible to efficient relaxation of its magnetisation through hyperfine, dipolar or other mechanisms.[18b]

The startling absence of other 'zero-field' Yb(III) SMMs may also be related to the design of Yb(III) SMMs based on ligand field environments and geometries which complement other 'prolate ions' such as Er(III).[19,20] Whilst both Yb(III) and Er(III) are both described as prolate, the 4f charge density approximations of the larger m_J states clearly possess different profiles.[21] This may begin to explain why many Yb(III) complexes based on either Er(III) SMMs or geometries that favour strictly prolate ions, produce only modest U_{eff} barriers and regularly require an applied dc field to observe slow magnetic relaxation.[22–26]

The 4f charge density approximation of the Yb(III) m_J states may also suggest a third possible reason for the efficient magnetic relaxation in Yb(III) SMMs.[21] Small changes in the local symmetry of Ln(III) ions are known to rapidly introduce transverse crystal field parameters (CFPs).[27,28] These transverse CFPs result in a mixing of m_J states and the introduction of

[a]*School of Chemistry, University of Glasgow, University Avenue, Glasgow G12 8QQ, UK. E-mail: mark.murrie@glasgow.ac.uk*
[b]*Department of Chemistry, Indian Institute of Technology Bombay, Powai, Mumbai, Maharashtra 400076, India. E-mail: rajaraman@chem.iitb.ac.in*

rapid magnetic relaxation through mechanisms such as quantum tunnelling of the magnetisation (QTM).[29–31]

One powerful way to control the local symmetry and distortions around a Ln(III) ion is to modify the second coordination sphere.[32,33] Second coordination sphere modifications have been shown to significantly change the magnetic properties of many SMMs through a variety of interactions.[34,35]

In this work we propose to utilise the inherent point group symmetry of two different anions; the octahedral (O_h) PF_6^- anion and the tetrahedral (T_d) $[BPh_4]^-$ anion. By replacing the $[BPh_4]^-$ anion with the PF_6^- anion we break the tetragonal crystallographic symmetry of the compound, generating distortions within the primary coordination sphere. As such we investigate the structural and magnetic properties of $[YbCl_2(Ph_3AsO)_4]BPh_4$ (**1**) and $[YbCl_2(Ph_3AsO)_4]PF_6$ (**2**) and employ computational studies to probe ground state composition, crystal field splitting and possible relaxation mechanisms.

Experimental

$[YbCl_2(Ph_3AsO)_4]BPh_4$ (1)

To a colourless solution of triphenylarsine oxide (0.4 mmol, 128.9 mg) and sodium tetraphenylborate (0.1 mmol, 34.2 mg) in ethanol (5 mL), warmed to 70 °C, was added ytterbium(III) chloride hexahydrate (0.1 mmol, 38.7 mg). The mixture was stirred for 1 h at 70 °C, quickly forming a white precipitate. While still warm, the solution was filtered through filter paper and the white solid was collected and dried. Once dry, the solid was dissolved in dichloromethane (5 mL), filtered through cotton wool, and the filtrate was used for layer and vapour diffusions with diethyl ether. Colourless block-like crystals suitable for single-crystal X-ray diffraction were obtained from vapour diffusion and confirmed to be $[YbCl_2(Ph_3AsO)_4]BPh_4$. The crystals were isolated and washed with Et_2O and dried, yielding 96.1 mg (52% yield) of the product. Elemental analysis calculated % for $[YbCl_2(Ph_3AsO)_4]BPh_4$ C: 62.3%, H: 4.4%, N: 0%, found: C: 62.1%, H: 4.4%, N: 0%. IR: $\bar{\nu}$ (cm^{-1}): 681, 732, 901, 962, 1086, 1437, 1479, 1580, 1977, 2019, 2161, 3050.

$[YbCl_2(Ph_3AsO)_4]PF_6$ (2)

To a solution of triphenylarsine oxide (0.4 mmol, 128.9 mg) and sodium hexafluorophosphate (0.1 mmol, 16.8 mg) in ethanol (5 mL), warmed to 70 °C, was added ytterbium(III) chloride hexahydrate (0.1 mmol, 38.7 mg). The mixture was stirred for 1 h at 70 °C, quickly forming a white precipitate. While still warm, the solution was filtered through filter paper and the solid was collected and dried. Once dry, the solid was dissolved in dichloromethane (5 mL), filtered through cotton wool, and the filtrate was used for layer and vapour diffusions with diethyl ether. Colourless block-like crystals suitable for single-crystal X-ray diffraction were obtained from vapour diffusion and confirmed to be $[YbCl_2(Ph_3AsO)_4]PF_6$. The crystals were isolated and washed with Et_2O and dried, yielding 114.1 mg (68% yield) of the product. Elemental analysis calculated % for $[YbCl_2(Ph_3AsO)_4]PF_6$ C: 51.5%, H: 3.6%, N: 0%, found: C: 51.4%, H: 3.6%, N: 0%. IR: $\bar{\nu}$ (cm^{-1}): 684, 738, 835, 897, 996, 1087, 1186, 1320, 1439, 1480, 1580, 2328, 2369, 3058.

Results and discussion

Crystal structures

$[YbCl_2(Ph_3AsO)_4]BPh_4$ (**1**) crystallises in the tetragonal space group $I4_1/a$ and $[YbCl_2(Ph_3AsO)_4]PF_6$ (**2**) crystallises in the lower symmetry triclinic space group $P\bar{1}$ (Fig. 1). One quarter of the $[Yb(Ph_3AsO)_4Cl_2]^+$ cation and one quarter of the $[BPh_4]^-$ anion are found within the asymmetric unit of **1**, whilst one full $[Yb(Ph_3AsO)_4Cl_2]^+$ cation and one PF_6^- anion are located in the asymmetric unit of **2**. The increase in the asymmetric unit in **2** is attributed to the introduction of the PF_6^- anion, which is found in an octahedral environment, and the misalignment of the primary rotational axes of the $[Yb(Ph_3AsO)_4Cl_2]^+$ and PF_6^- ions. This results in a breaking of tetragonal symmetry within the crystal lattice of **2** (*vide infra*).

Similar average axial Yb–Cl bond lengths of 2.641 Å and 2.633(1) Å are observed for **1** and **2**, respectively. However, **2** possesses two differing Yb–Cl bond lengths (2.626(1) Å and 2.640(1) Å), already indicating an increased distortion in **2**. Axial Cl–$\widehat{Yb}$–Cl angles of 180° in **1** and 176.24(4)° in **2** further highlights the increased distortion in **2**. The perfectly linear 180° Cl–$\widehat{Yb}$–Cl angle in **1** is enforced by the four-fold rotoinversion axis that lies along the Cl–$\widehat{Yb}$–Cl bond (Fig. 2). Equatorial Yb–O bond lengths observed in **1** (2.163 Å) and **2** (2.190(3),

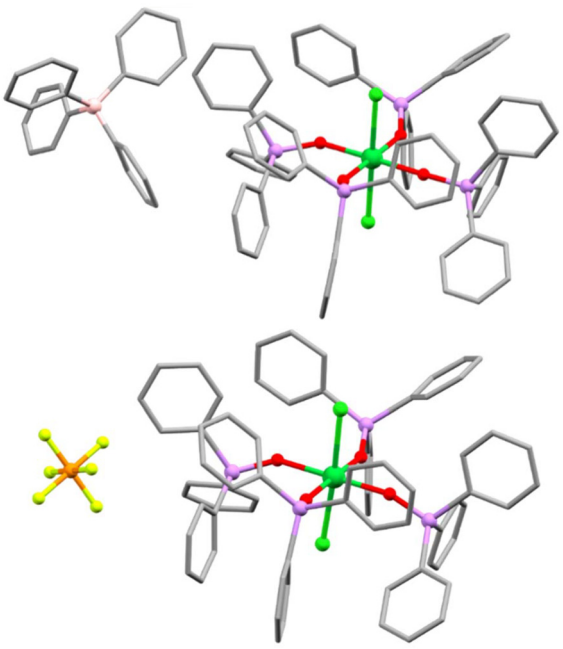

Fig. 1 The structure of compounds **1** (top) and **2** (bottom). As, purple; B, pink; C, grey; Cl, light green; F, yellow; O, red; P, orange; Yb, green; with H atoms omitted for clarity.

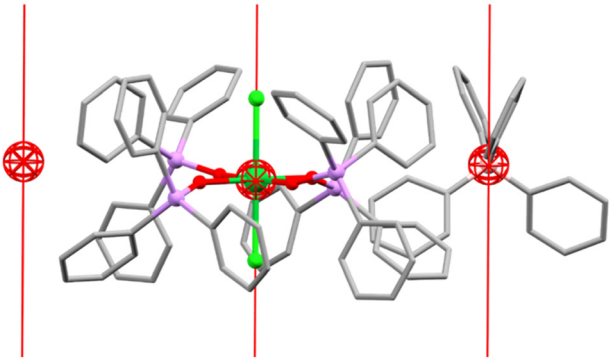

Fig. 2 The structure of **1** highlighting the S_4 rotoinversion axes (red lines). As, purple; B, pink; C, grey; Cl, light green; O, red; Yb, green; with H atoms omitted for clarity.

2.174(3), 2.166(3) and 2.168(3) Å) again highlight the increased distortion of the $\{YbO_4Cl_2\}$ unit present in **2**.

Both Yb(III) centres are determined to have distorted octahedral geometry (O_h) by continuous shape measures analysis (CShMs) (0.942 for **1** and 0.898 for **2**).[36] It should be noted that CShMs does not produce a score for a D_{4h} geometry and the elongation of the axial Yb–Cl bonds means that a better description for the structure of the Yb(III) centres in **1** and **2** is *pseudo*-D_{4h}. This also explains the unusual reduction in the O_h CShMs value for **2**, which displays the more distorted structure. A slight elongation of the axial bonds in **1** likely results in the larger O_h CShMs score. To give a better representation of the equatorial distortion in **2** caused by the loss of tetragonal symmetry, we investigated the D_{4h} CShMs score for the square planar fragment $\{YbO_4\}$ (Fig. S1). Compound **1** $\{YbO_4\}$ gives a D_{4h} CShMs value of 0.004 whilst **2** $\{YbO_4\}$ gives a D_{4h} CShMs value 0.019. This is equivalent to a roughly five-fold increase in equatorial distortion in compound **2**.

Furthermore, investigation of the S_4 symmetry operation using continuous symmetry measures reveals a deviation away from perfect S_4 symmetry in the $\{YbO_4Cl_2\}$ unit of compound **2**.[36b] This is characterised by the increased continuous symmetry measure (CSM) for the S_4 symmetry operation of 0.0310 for **2** *vs.* 0 for compound **1**, which possesses an ideal S_4 axis. In the crystal packing of compound **1**, *pseudo*-2D layers arise from intermolecular edge-to-face interactions between phenyl rings of the $OAsPh_3$ ligand and the $[BPh_4]^-$ anion ($C_{centroid}\cdots C$, 3.58 and 3.86 Å) (Fig. 3). The shortest intermolecular Yb(III)···Yb(III) distances of 11.67 Å occur between both staggered and head-to-tail complexes which crystallise along the crystallographic *c*-axis (Fig. 3). Intermolecular π–π interactions between phenyl ($OAsPh_3$) rings of neighbouring complexes (C···C, 3.43–3.62 Å) alongside interactions between the phenyl rings of $OAsPh_3$ and the PF_6^- anion (C···F, 3.04–3.51 Å) also afford complex **2** a similar *pseudo*-2D layer structure and packing as observed in **1** (Fig. 4). The nearest intermolecular Yb(III)···Yb(III) distance of 10.88 Å occurs between staggered molecules within different layers along the crystallographic

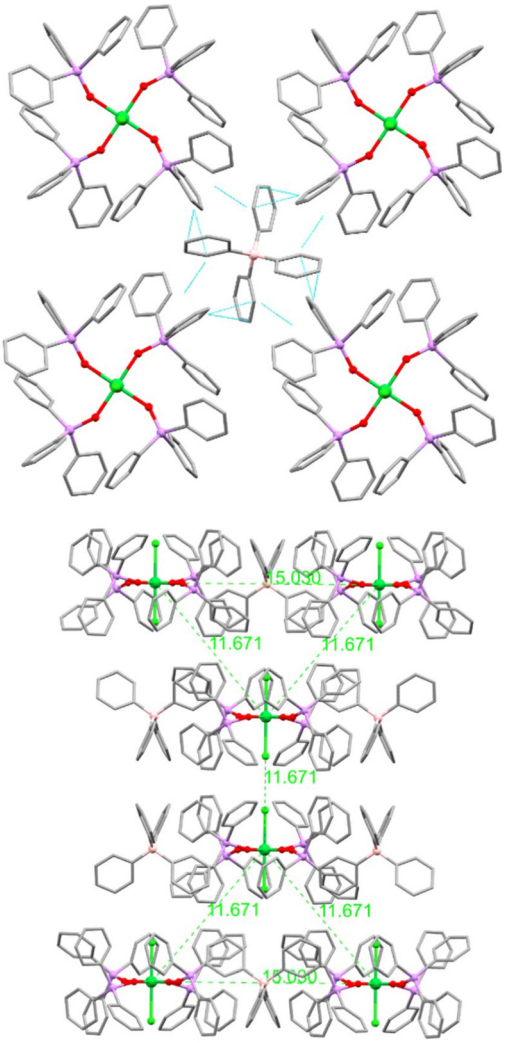

Fig. 3 The crystal packing of **1** looking along the crystallographic *c*-axis, highlighting the intermolecular interactions between complexes in the same layer (top). The crystal packing between layers in **1** looking down the crystallographic *b*-axis, where the Yb(III)···Yb(III) distances are in green (bottom). As, purple; B, pink; C, grey; Cl, light green; O, red; Yb, green; with H atoms omitted for clarity.

a-axis (Fig. 4). The phase purity of compounds **1** and **2** was confirmed by powder X-ray diffraction (Fig. S2).

The significant difference in space group between **1** ($I4_1/a$) and **2** ($P\bar{1}$) can be rationalised by considering not only the structure of the anions, but also their orientation and intermolecular interactions with the $[Yb(Ph_3AsO)_4Cl_2]^+$ cations. Incorporation of a large $[BPh_4]^-$ anion in **1** results in highly directional edge-to-face interactions with only the equatorial component of the SIM unit. As such, the $[BPh_4]^-$ anion is locked into a pre-determined orientation. This reduced rotational degree of freedom results in an alignment of the S_4 axes (Fig. 2) and the perpetuation of tetragonal symmetry throughout the crystal lattice. Conversely, the smaller size, higher symmetry and weak intermolecular interactions of the PF_6^- anion result in a much greater rotational degree of freedom in **2**. The PF_6^- anion acts as an effective

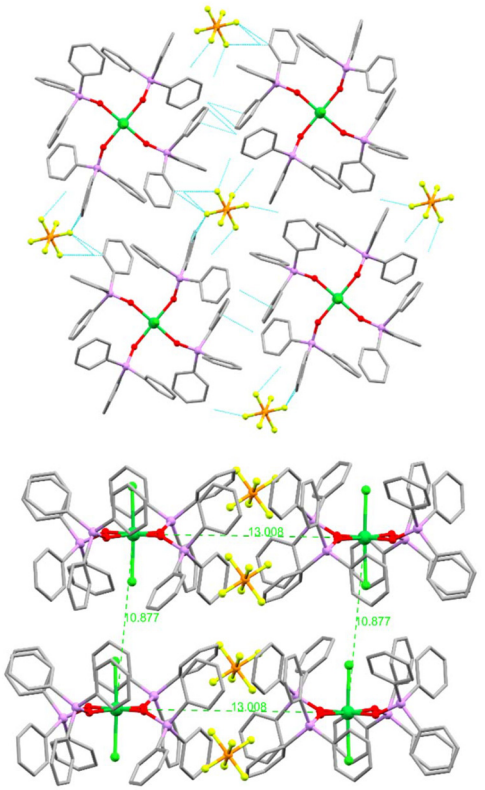

Fig. 4 The crystal packing of **2** highlighting the intermolecular interactions between complexes and PF_6^- anions in the same layer (top). The crystal packing between layers in **2** showing the closest intra-layer and inter-layer intermolecular Yb(III)···Yb(III) distances in Å (bottom). As, purple; C, grey; Cl, light green; F, yellow; O, red; P, orange; Yb, green; with H atoms omitted for clarity.

spherical charge with only a limited directional dependence. As such, both molecules are orientated where their ~C_2 Cl–$\widehat{Yb}$–Cl axes are mis-aligned, resulting in the absence of a C_2 crystallographic axis in the crystal structure of **2**. Whilst controlling crystal packing is not trivial, a sound understanding of the geometry, symmetry and potential interactions between molecules can allow for a rational design of crystal structures with both high and low symmetry.

Magnetic characterisation

The magnetic properties of polycrystalline samples of **1** and **2**, suspended in eicosane, were measured in an applied dc field of 1000 Oe from 280–2 K (Fig. S3). The $\chi_M T$ values at 280 K for complexes **1** and **2**, of 2.33 and 2.45 $cm^3\ mol^{-1}$ K, respectively are slightly lower than the theoretical value (2.57 $cm^3\ mol^{-1}$ K). This slight decrease is attributed to ligand field effects[37,38] and the values are in excellent agreement with those observed in other Yb(III) SMMs.[39–41] Upon cooling, $\chi_M T$ decreases steadily for both compounds until reaching 1.57 and 1.68 $cm^3\ mol^{-1}$ K for **1** and **2**, respectively. This decrease is attributed to the depopulation of excited Stark states, where the uneven separation of the excited states explains the non-linear decrease across the temperature range.[42,43] Magnetisation *vs.* field measurements were conducted on **1** and **2** at 2, 4 and 6 K from 0–7 T (Fig. S4). At 2 K under an applied dc field of 7 T experimental magnetisation values (M_{exp}) of 1.82 and 1.94$N\beta$ are observed for **1** and **2**, respectively. These values are in good agreement with the expected M_{sat} value (≈2$N\beta$) for a highly anisotropic $m_J = \pm 7/2$ ground state (1/4 g_{zz}).[27]

Variable temperature ac susceptibility measurements were conducted on **1** and **2** to probe for the presence of slow magnetic relaxation. Neither complex displayed any out-of-phase (χ'') magnetic susceptibility peaks under zero applied field, likely a result of efficient QTM. To probe for field-induced slow magnetic relaxation, variable-field χ' and χ'' *vs.* frequency measurements were conducted from 0–4000 Oe, across a 1–941 Hz frequency range at 3 and 2 K for **1** and **2**, respectively (Fig. S5 and S6). Cole–Cole plots were then constructed from the χ' *vs.* χ'' data and fitted across a 200–4000 Oe range to a generalised Debye equation using CCFIT2 to obtain tau values.[44,45] The tau values were then plotted *vs.* applied dc field to obtain the optimum applied field for the suppression of QTM (Fig. S7). Both compounds display a similar field dependence of their tau values, characteristic of a suppression of QTM under small magnetic fields and the onset of direct relaxation at large fields. Optimum applied dc fields of 600 Oe and 1000 Oe were then selected to conduct variable-temperature ac susceptibility measurements for **1** and **2**, respectively.

Variable-temperature ac susceptibility measurements conducted from 2–15 K and 1–941 Hz under an applied field of 600 and 1000 Oe for compounds **1** and **2**, respectively, are shown in Fig. 5 and 6. Spikes in the data around 10.65 Hz are artefacts. Frequency dependant peaks in the χ'' data are present up to 3.75 K for both compounds, with a clear frequency dependence of χ' below 4 K. Cole–Cole plots were then constructed from the χ' and χ'' data and variable-temperature tau values were extracted by fitting the 2–3.75 K temperature range to a generalized Debye law using CCFIT2 (Fig. S8).[44,45]

Plotting of the relaxation rate (τ^{-1}) *vs.* temperature (Fig. 7) allows for the relaxation rate to be modelled and the extraction of the relaxation parameters using either Orbach and QTM or Raman and QTM relaxation mechanisms, using eqn (1) and (2):

$$\tau^{-1} = {\tau_{QTM}}^{-1} + CT^n; \quad (1)$$

$$\tau^{-1} = {\tau_{QTM}}^{-1} + {\tau_0}^{-1} \exp\left(-\frac{U_{eff}}{T}\right). \quad (2)$$

The parameters ${\tau_{QTM}}^{-1}$ = 196(9) s^{-1}, C = 1.0(1) $K^{-n}\ s^{-1}$ and n = 6.52(8) were obtained from fitting the tau values of **1** across a 2–3.75 K range using eqn (1). For **2**, the parameters ${\tau_{QTM}}^{-1}$ = 71(11) s^{-1}, C = 3.5(2) $K^{-n}\ s^{-1}$ and n = 5.40(4) were obtained using eqn (1). Attempts to model the relaxation rate using a direct process resulted in a poor quality of fit and unreasonable parameters. A decrease in ${\tau_{QTM}}^{-1}$ is observed in compound **2**, which is surprising due to its more distorted structure and shorter intermolecular Yb(III)···Yb(III) distances. However, the use of a larger applied dc magnetic field in the ac measurements is consistent with a decrease in ${\tau_{QTM}}^{-1}$ for **2**. Furthermore, a significant change in Raman relaxation is

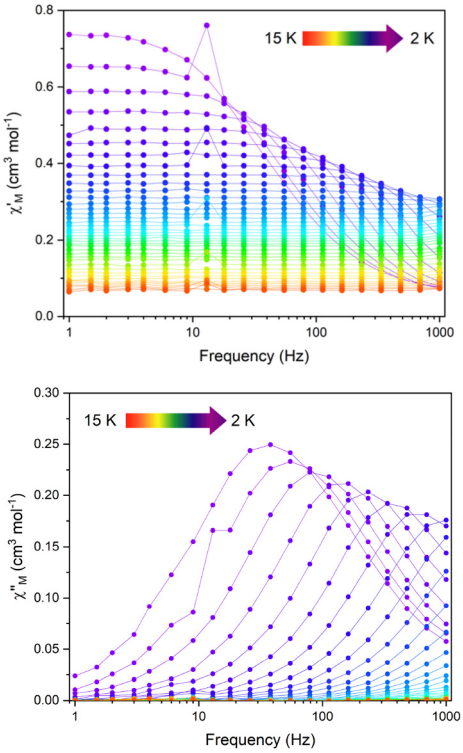

Fig. 5 The frequency dependence of the in-phase (top) and out-of-phase (bottom) ac susceptibility signals in the temperature range 2–15 K under an applied field of 600 Oe for **1**.

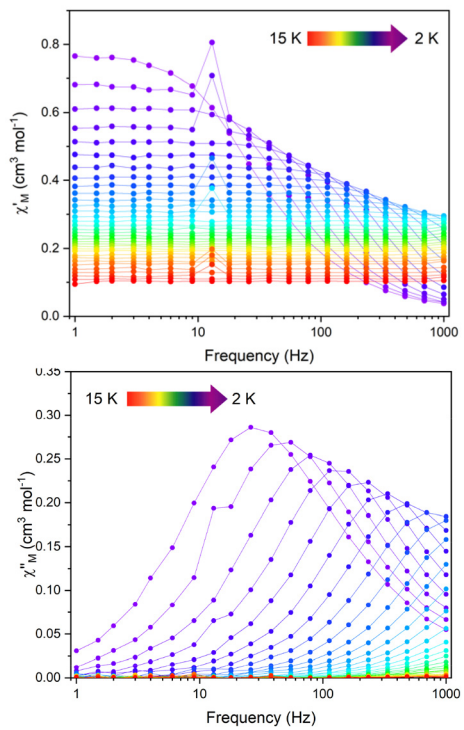

Fig. 6 The frequency dependence of the in-phase (top) and out-of-phase (bottom) ac susceptibility signals in the temperature range 2–15 K under an applied field of 1000 Oe for **2**.

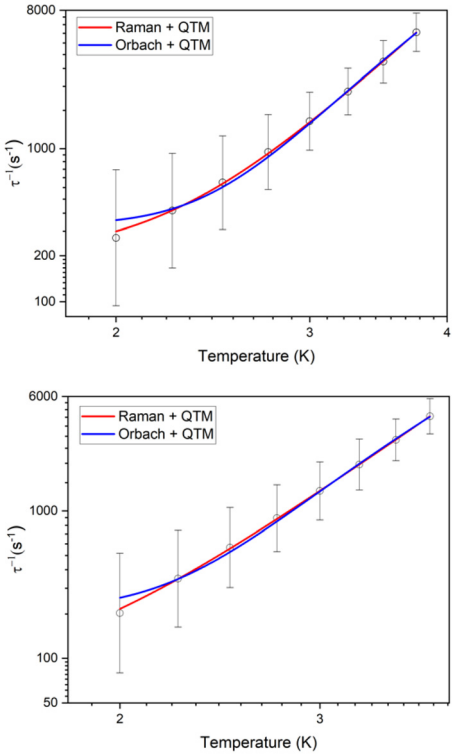

Fig. 7 The relaxation rates for **1** (top) and **2** (bottom) from 2–3.75 K where the red and blue lines represent the best fit to Raman + QTM or Orbach + QTM relaxation mechanisms, respectively (top). Black vertical bars are estimated standard deviations in the relaxation times derived from Debye fits according to ref. 44.

observed, as might be expected for a change in intermolecular packing and the introduction of an anion that possesses different Raman active vibrational modes.[46–48]

Alternatively, compounds **1** and **2** can be fitted using Orbach and QTM relaxation mechanisms and eqn (2). This fit produces a noticeably poorer fit at low temperatures (Fig. 7). However, at higher temperatures the Orbach mechanism provides an accurate fit to the tau values. The parameters obtained from the alternative fit for compounds **1** and **2** are τ_{QTM}^{-1} = 316(41) s^{-1}, U_{eff} = 23.2(8) K and τ_0 = 3.8(8) × 10^{-7} s and τ_{QTM}^{-1} = 213(32) s^{-1}, U_{eff} = 19.4(6) K, and τ_0 = 1.4(2) × 10^{-6} s, respectively. A summary of all extracted parameters can be found in Table 1.

Table 1 A comparison of the QTM, Raman and Orbach parameters extracted from the different fits of the relaxation rates for compounds **1** and **2**

	Raman + QTM			Orbach + QTM		
	C (K^{-n} s^{-1})	n	τ_{QTM}^{-1} (s^{-1})	U_{eff} (K)	$\tau_0 \times 10^{-7}$ (s)	τ_{QTM}^{-1} (s^{-1})
1	1.0(1)	6.52(8)	196(9)	23.2(8)	3.8(8)	316(41)
2	3.5(2)	5.40(4)	71(11)	19.4(6)	14(2)	213(32)

A small increase in U_{eff} observed in **1** could be attributed to an increased crystal field splitting resulting from the tetragonal symmetry imposed by the $[BPh_4]^-$ anion. However, from the magnetic data alone it is impossible to discern whether Raman or Orbach relaxation are observed in compounds **1** and **2**. However, as Orbach relaxation is only permitted to proceed through a 'real state', *ab initio* calculations were conducted to determine the crystal field splitting of the Kramers doublets and probe for the presence of a real Kramers doublet around 20 K.

Theoretical studies

The *ab initio* calculations for estimating the spin Hamiltonian parameters have been performed using the MOLCAS programme package.[49] SINGLE_ANISO[50] calculations were carried out to determine the *g*-tensors of the low-lying eight Kramers Doublets (KDs). The U_{cal} values, *g* factor anisotropy, crystal field parameters and the direction of g_{zz} of the ground KD were extracted. The energy distribution of the m_J states, composition of the m_J states, *g* tensors and angle of the excited state g_{zz} tensors with respect to the ground g_{zz} tensor of **1** and **2** are shown in Table 2.

The four Kramers doublets in the $^2F_{7/2}$ ground state of **1** span 699 cm^{-1}. The ground state comprises relatively pure m_J = ±7/2 states with a small contribution from the m_J = ±5/2 states (Table 2). The ground Kramers doublet also possesses only small transverse *g* tensor components (g_{xx} = 0.165, g_{yy} = 0.343) with g_{zz} = 7.455, which generates a large axial magnetic anisotropy. Whilst the excited KDs (2–4) possess highly admixed states and significant transverse anisotropy, the g_{zz} angles remain highly collinear with the ground state. This is attributed to the high degree of axial symmetry within **1** (*vide supra*).

The four Kramers doublets in the $^2F_{7/2}$ ground state of **2** span 679 cm^{-1}, similar to the splitting in **1**. A small decrease in the purity of the ground state is observed (94% ± 7/2 in **1** and 91% ± 7/2 in **2**), with an increased contribution from the more oblate m_J = ±1/2 states. This can be rationalised by the increased distortion in **2** which generates larger calculated transverse crystal field parameters (see Table S5) resulting in an increased admixture of m_J states. The ground Kramers doublet possesses a large magnetic anisotropy with g_{zz} = 7.500 and small transverse g_{xx} = 0.121 and g_{yy} = 0.335 terms, similar to **1**. Most notable is the decrease in collinearity of the excited KD g_{zz} tensors with the ground state g_{zz} tensor, compared to **1**. This indicates that the breaking of tetragonal symmetry in **2** generates a significant loss of axiality in the excited states, which has been attributed to faster relaxation of the magnetisation in a number of SMMs. As such, symmetry enforcing of perfect L–Yb–L bond angles is an important route to generate SMMs that display strong axiality throughout the excited Kramers doublets.

The g_{zz} anisotropy axis is aligned along the Cl–Yb–Cl (180°) axis coincident with the S_4 rotoinversion axis in **1**, whereas in **2** the g_{zz} anisotropy axis deviates from the Cl–Yb–Cl (~176°) axis (Fig. 8). In **1** and **2** the first excited Kramers doublets at

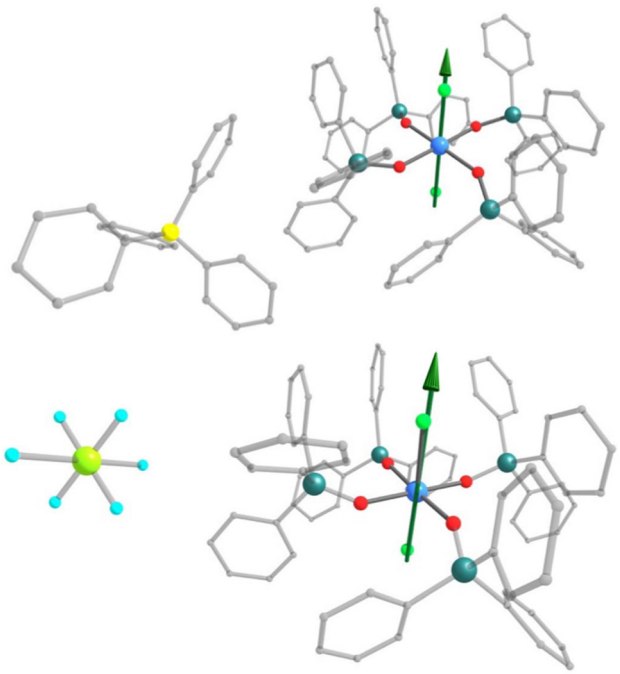

Fig. 8 The calculated anisotropy axis (dark green arrow) of the ground state Kramers doublet of **1** (top) and **2** (bottom), where As, green-blue; B, yellow; C, grey; Cl, light green; F, cyan; O, red; P, lime; Yb, blue; with H atoms omitted for clarity.

Table 2 The energy distribution and composition of the states, *g* tensors and angle of the excited state g_{zz} tensors with respect to the ground g_{zz} tensor of compounds **1** and **2**

Multiplet	Energy (cm^{-1})	Composition	g_{xx}	g_{yy}	g_{zz}	Angle with the ground state
Compound **1**						
1	0.0	0.94 |±7/2⟩ + 0.06 |±5/2⟩	0.165	0.343	7.455	—
2	429.0	0.63 |±5/2⟩ + 0.37 |±3/2⟩	3.994	3.607	2.315	0.01
3	600.2	0.06 |±7/2⟩ + 0.93 |±1/2⟩	4.566	4.045	0.657	0.1
4	698.9	0.37 |±5/2⟩ + 0.63 |±3/2⟩	3.970	3.645	0.085	0.1
Compound **2**						
1	0.0	0.91 |±7/2⟩ + 0.05 |±1/2⟩	0.121	0.335	7.500	—
2	430.8	0.62 |±5/2⟩ + 0.36 |±3/2⟩	3.951	3.664	2.298	6.7
3	578.8	0.92 |±1/2⟩	5.092	3.527	0.662	2.4
4	679.1	0.36 |±5/2⟩ + 0.62 |±3/2⟩	4.600	3.054	0.042	4.2

429 and 431 cm^{-1} are an admixture of the ±5/2 and ±3/2 m_J states and possesses a significant transverse contribution (g_{xx} = 3.994, g_{yy} = 3.607 for **1** and g_{xx} = 3.951, g_{yy} = 3.664 for **2**). Despite the collinear anisotropy axis of the first excited Kramers doublet in **1**, the large transverse anisotropy indicates that relaxation of the magnetisation cannot proceed through an energy barrier larger than the splitting between the ground and first excited Kramers doublet. This gives rise to a large U_{cal} value of 429 cm^{-1} (Fig. 9). Compound **2** also displays significant transverse anisotropy and a decrease in collinearity in the first excited Kramers doublet, with a similar U_{cal} value of 431 cm^{-1}.

In both compounds, relaxation of the magnetisation is predicted to proceed through the first excited Kramers doublet (Fig. 9). However, this does not correlate well with the absence of signal in the out-of-phase magnetic susceptibility under no external applied field. This indicates that other factors contribute towards a fast relaxation of the magnetic moment in **1** and **2**. Under an applied magnetic field, the extracted U_{eff} barriers of 23.2(8) and 19.4(6) K for **1** and **2**, respectively are far too small compared to the calculated splitting of the Kramers doublets and U_{cal}. It should be noted that the crystal field states for Yb(III) are generally overestimated in the computational methodology employed, as seen in other Yb(III) complexes,[23] and that there is significant transverse anisotropy that will reduce the calculated barrier height due to QTM. Nevertheless, the absence of a real m_J state around 20 K indicates that Raman relaxation is likely the dominant mechanism controlling magnetic relaxation in **1** and **2**. This is consistent with the use of Raman and QTM to fit the dynamic magnetic data in **1** and **2** and suggests that these Yb(III) complexes display highly efficient Raman relaxation.

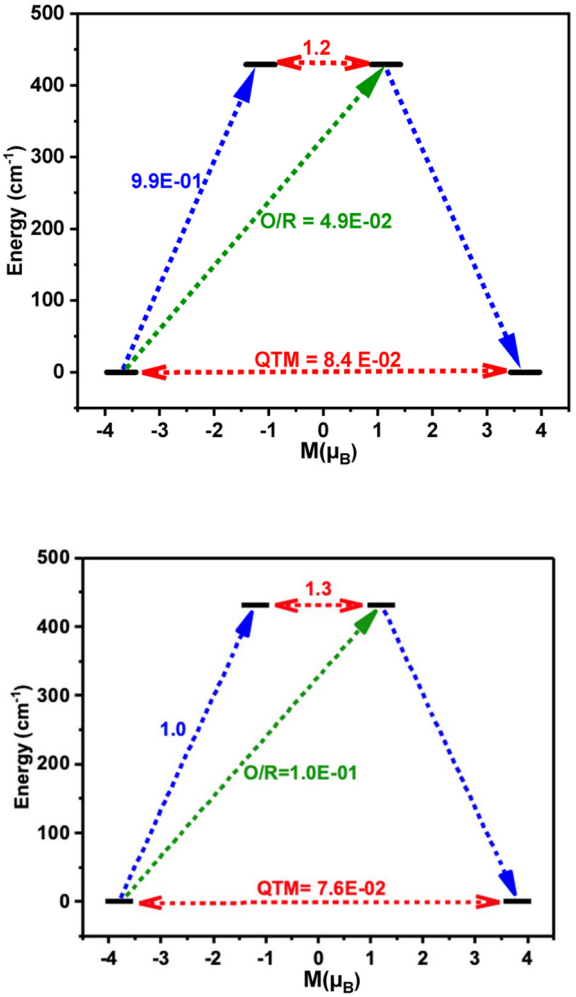

Fig. 9 *Ab initio* calculated relaxation dynamics and energy splitting between the ground and first excited Kramers doublets for **1** (top) and **2** (bottom). The arrows show the connected energy states and the accompanying number represents the transverse matrix element for the transition magnetic moments. Where QTM = red, Orbach/Raman = green, Orbach = blue.

Conclusions

We have demonstrated that by judicious choice of anion, it is possible to generate high symmetry Yb(III) SMMs. The alignment of the molecular S_4 axes of both $[Yb(Ph_3AsO)_4Cl_2]^+$ and $[BPh_4]^-$ molecules generates a tetragonal crystal lattice and enforces a perfectly linear Cl–Yb–Cl bond angle within the SMM unit of **1**, aligning the anisotropy axis of the first excited Kramers doublet in particular. Whilst the breaking of tetragonal symmetry in compound **2** does not lead to drastic changes in the observed slow magnetic relaxation, a significant decrease in the *ab initio* calculated collinearity of the anisotropy axes of the excited Kramers doublets is observed, alongside a change in the ground m_J = ±7/2 state composition with a small admixture of the m_J = ±1/2 states.

Even with the 180° Cl–Yb–Cl angle and very small distortion of the equatorial ligand field in **1**, the calculated relaxation barrier (U_{cal} ~ 430 cm^{-1}) is not observed. We suggest that this is due to a highly efficient Raman relaxation, that occurs in compounds **1** and **2**. Many Yb(III) complexes display a similar relaxation profile to **1** and **2**, hinting that Yb(III) ions may be highly susceptible to Raman relaxation or, as proposed by other groups, other efficient relaxation mechanisms. This may indicate that a suitable ligand field has not been found to complement the unusual electron density distribution of the m_J = +7/2 state. The identification and suppression of this relaxation mechanism now proves the next major hurdle to overcome in the search for high-performance Yb(III) SMMs. Nonetheless, we propose that symmetry enforcing of perfect L–Ln–L bond angles, through careful anion selection, may prove a powerful strategy for obtaining future high-performance Yb(III) SMMs.

Author contributions

EL and HH carried out the synthesis, sample characterisation, magnetic measurements and data analysis, advised by MM. EL

and SD carried out the crystallographic measurements and data analysis, advised by CW. Calculations were carried out by TS, advised by GR. MM and EL devised and supervised the project. The manuscript was written by EL and MM with input from all authors.

Conflicts of interest

There are no conflicts to declare.

Data availability

Supplementary information: experimental section, crystallographic details, magnetic and computational studies. See DOI: https://doi.org/10.1039/d5dt01565k.

CCDC 2469525 and 2469526 contain the supplementary crystallographic data for this paper.[51a,b]

Acknowledgements

MM thanks EPSRC UK (EP/T517896/1) for funding. GR thanks DST/SERB (SB/SJF/2019-20/12; CRG/2022/001697) for funding.

References

1 C. A. P. Goodwin, F. Ortu, D. Reta, N. F. Chilton and D. P. Mills, *Nature*, 2017, **548**, 439–442.
2 F.-S. Guo, B. M. Day, Y.-C. Chen, M.-L. Tong, A. Mansikkamäki and R. A. Layfield, *Science*, 2017, **362**, 1400–1403.
3 W. Xu, Q. Luo, Z. Li, Y. Zhai and Y. Zheng, *Adv. Sci.*, 2024, **11**, 2308548.
4 J. Liu, Y.-C. Chen, J.-L. Liu, V. Vieru, L. Ungur, J.-H. Jia, L. F. Chibotaru, Y. Lan, W. Wernsdorfer, S. Gao, X.-M. Chen and M.-L. Tong, *J. Am. Chem. Soc.*, 2016, **138**, 5441–5450.
5 Y. Ding, T. Han, Y. Zhai, D. Reta, N. F. Chilton, R. E. P. Winpenny and Y. Zheng, *Chem. – Eur. J.*, 2020, **26**, 5893–5902.
6 A. B. Canaj, S. Dey, C. Wilson, O. Céspedes, G. Rajaraman and M. Murrie, *Chem. Commun.*, 2020, **56**, 12037–12040.
7 N. Ishikawa, M. Sugita, T. Ishikawa, S.-y. Koshihara and Y. Kaizu, *J. Am. Chem. Soc.*, 2003, **125**, 8694–8695.
8 Y. Chen, F. Ma, X. Chen, B. Dong, K. Wang, S. Jiang, C. Wang, X. Chen, D. Qi, H. Sun, B. Wang, S. Gao and J. Jiang, *Inorg. Chem.*, 2017, **56**, 13889–13896.
9 M. G. Bernbeck, A. P. Orlova, J. D. Hilgar, M. Gembicky, M. Ozerov and J. D. Rinehart, *J. Am. Chem. Soc.*, 2024, **146**, 7243–7256.
10 A. P. Orlova, M. S. Varley, M. G. Bernbeck, K. M. Kirkpatrick, P. C. Bunting, M. Gembicky and J. D. Rinehart, *J. Am. Chem. Soc.*, 2023, **145**, 22265–22275.
11 Y. Duan, L. E. Rosaleny, J. T. Coutinho, S. Giménez-Santamarina, A. Scheie, J. J. Baldoví, S. Cardona-Serra and A. Gaita-Ariño, *Nat. Commun.*, 2022, **13**, 7626.
12 H. Kwon, K. R. McClain, J. G. C. Kragskow, J. K. Staab, M. Ozerov, K. R. Meihaus, B. G. Harvey, E. S. Choi, N. F. Chilton and J. R. Long, *J. Am. Chem. Soc.*, 2024, **146**, 18714–18721.
13 S. K. Gupta, T. Rajeshkumar, G. Rajaraman and R. Murugavel, *Chem. Commun.*, 2016, **52**, 7168–7171.
14 J. Chen, T.-D. Zhou and W. Sun, *Dalton Trans.*, 2023, **52**, 4643–4657.
15 Y. Liu, B.-H. Lyu, S.-N. Du, G.-Z. Huang, Z.-Y. Ruan, S.-G. Wu, J.-L. Liu and M.-L. Tong, *Dalton Trans.*, 2021, **50**, 6778–6783.
16 R. Marin, G. Brunet and M. Murugesu, *Angew. Chem., Int. Ed.*, 2021, **60**, 1728–1746.
17 M. J. Klein, *Am. J. Phys.*, 1952, **20**, 65–71.
18 (*a*) J. Flores Gonzalez, H. Douib, B. Le Guennic, F. Pointillart and O. Cador, *Inorg. Chem.*, 2021, **60**, 540–544; (*b*) K. S. Pedersen, J. Dreiser, H. Weihe, R. Sibille, H. V. Johannesen, M. A. Sørensen, B. E. Nielsen, M. Sigrist, H. Mutka, S. Rols, J. Bendix and S. Piligkos, *Inorg. Chem.*, 2015, **54**, 7600–7606.
19 G. K. Gransbury, H. M. Nicholas, S. R. Murphy, J. Emerson-King, M. Vonci, C. A. P. Goodwin, R. E. P. Winpenny, N. F. Chilton, M. J. Giansiracusa and D. P. Mills, *Inorg. Chem.*, 2024, **63**, 22422–22434.
20 K. R. Meihaus and J. R. Long, *J. Am. Chem. Soc.*, 2013, **135**, 17952–17957; P. Zhang, L. Zhang, C. Wang, S. Xue, S.-Y. Lin and J. Tang, *J. Am. Chem. Soc.*, 2014, **136**, 4484–4487.
21 J. D. Rinehart and J. R. Long, *Chem. Sci.*, 2011, **2**, 2078–2085.
22 J. Wang, J. J. Zakrzewski, M. Heczko, M. Zychowicz, K. Nakagawa, K. Nakabayashi, B. Sieklucka, S. Chorazy and S.-i. Ohkoshi, *J. Am. Chem. Soc.*, 2020, **142**, 3970–3979.
23 A. Borah, S. Dey, S. K. Gupta, M. G. Walawalkar, G. Rajaraman and R. Murugavel, *Chem. Commun.*, 2020, **56**, 11879–11882.
24 K. Soussi, J. Jung, F. Pointillart, B. Le Guennic, B. Lefeuvre, S. Golhen, O. Cador, Y. Guyot, O. Maury and L. Ouahab, *Inorg. Chem. Front.*, 2015, **2**, 1105–1117.
25 S. P. Petrosyants, K. A. Babeshkin, A. V. Gavrikov, A. B. Ilyukhin, E. V. Belova and N. N. Efimov, *Dalton Trans.*, 2019, **48**, 12644–12655.
26 P.-H. Lin, W.-B. Sun, Y.-M. Tian, P.-F. Yan, L. Ungur, L. F. Chibotaru and M. Murugesu, *Dalton Trans.*, 2012, **41**, 12349.
27 J.-L. Liu, Y.-C. Chen and M.-L. Tong, *Chem. Soc. Rev.*, 2018, **47**, 2431–2453.
28 D. N. Woodruff, R. E. P. Winpenny and R. A. Layfield, *Chem. Rev.*, 2013, **113**, 5110–5148.
29 A. B. Canaj, S. Dey, E. R. Martí, C. Wilson, G. Rajaraman and M. Murrie, *Angew. Chem., Int. Ed.*, 2019, **58**, 14146–14151.

30 S. Liu, Y. Gil, C. Zhao, J. Wu, Z. Zhu, X.-L. Li, D. Aravena and J. Tang, *Inorg. Chem. Front.*, 2022, **9**, 4982–4989.
31 P. K. Sahu, A. Mondal and S. Konar, *Chem. – Eur. J.*, 2023, **29**, e202203664.
32 E. Lowe, C. Wilson, A. B. Canaj and M. Murrie, *Dalton Trans.*, 2025, **54**, 477–481; A. B. Canaj, M. K. Singh, C. Wilson, G. Rajaraman and M. Murrie, *Chem. Commun.*, 2018, **54**, 8273–8276.
33 R. Herchel, P. Zoufalý and I. Nemec, *RSC Adv.*, 2019, **9**, 569–575.
34 S. S. Leiszner, M. Perfetti, E. Damgaard-Møller, Y.-S. Chen and B. B. Iversen, *Dalton Trans.*, 2024, **53**, 19246–19255.
35 Y. Gil, L. Llanos, P. Cancino, P. Fuentealba, A. Vega, E. Spodine and D. Aravena, *J. Phys. Chem. C*, 2020, **124**, 5308–5320.
36 (*a*) M. Pinsky and D. Avnir, *Inorg. Chem.*, 1998, **37**, 5575–5582; (*b*) G. Alon and I. Tuvi-Arad, *J. Math. Chem.*, 2018, **56**, 193–212.
37 O. A. Blackburn, R. M. Edkins, S. Faulkner, A. M. Kenwright, D. Parker, N. J. Rogers and S. Shuvaev, *Dalton Trans.*, 2016, **45**, 6782–6800.
38 D. Parker, E. A. Suturina, I. Kuprov and N. F. Chilton, *Acc. Chem. Res.*, 2020, **53**, 1520–1534.
39 S. Chorazy, M. Rams, J. Wang, B. Sieklucka and S.-i. Ohkoshi, *Dalton Trans.*, 2017, **46**, 13668–13672.
40 A. V. Gavrikov, A. Ilyukhin, I. V. Taydakov, M. T. Metlin, N. Datskevitch, M. E. Buzoverov, K. A. Babeshkin and N. N. Efimov, *Dalton Trans.*, 2023, **52**, 17911–17927.
41 X. Yi, K. Bernot, V. Le Corre, G. Calvez, F. Pointillart, O. Cador, B. Le Guennic, J. Jung, O. Maury, V. Placide, Y. Guyot, T. Roisnel, C. Daiguebonne and O. Guillou, *Chem. – Eur. J.*, 2014, **20**, 1569–1576.
42 D. Gatteschi and C. Benelli, *Introduction to Molecular Magnetism: From Transition Metals to Lanthanides*, Wiley-VCH, 2015.
43 M. L. Kahn, C. Mathonière and O. Kahn, *Inorg. Chem.*, 1999, **38**, 3692–3697.
44 D. Reta and N. F. Chilton, *Phys. Chem. Chem. Phys.*, 2019, **21**, 23567–23575.
45 W. J. A. Blackmore, G. K. Gransbury, P. Evans, J. G. C. Kragskow, D. P. Mills and N. F. Chilton, *Phys. Chem. Chem. Phys.*, 2023, **25**, 16735–16744.
46 G. Handzlik, M. Magott, M. Arczyński, A. M. Sheveleva, F. Tuna, S. Baran and D. Pinkowicz, *Dalton Trans.*, 2020, **49**, 11942–11949.
47 W. Huang, R. A. Wheeler and R. Frech, *Spectrochim. Acta, Part A*, 1994, **50**, 985–996.
48 X. Xuan, J. Wang and H. Wang, *Electrochim. Acta*, 2005, **50**, 4196–4201.
49 G. Karlström, R. Lindh, P.-Å. Malmqvist, B. O. Roos, U. Ryde, V. Veryazov, P.-O. Widmark, M. Cossi, B. Schimmelpfennig, P. Neogrady and L. Seijo, *Comput. Mater. Sci.*, 2003, **28**, 222–239.
50 L. F. Chibotaru and L. Ungur, *J. Chem. Phys.*, 2012, **137**, 064112.
51 (*a*) E. Lowe, H. Hourston, T. Sharma, S. K. Dugmore, C. Wilson, G. Rajaraman and M. Murrie, CCDC 2469525 (**1**): Experimental Crystal Structure Determination, 2025, DOI: **10.5517/ccdc.csd.cc2nwr3f**; (*b*) E. Lowe, H. Hourston, T. Sharma, S. K. Dugmore, C. Wilson, G. Rajaraman and M. Murrie, CCDC 2469526 (**2**): Experimental Crystal Structure Determination, 2025, DOI: **10.5517/ccdc.csd.cc2nwr4g**.